

pubs.acs.org/Macromolecules Article

Leveraging Sequential Doping of Semiconducting Polymers to Enable Functionally Graded Materials for Organic Thermoelectrics

Tengzhou Ma, Ban Xuan Dong, Garrett L. Grocke, Joseph Strzalka, and Shrayesh N. Patel*



Cite This: Macromolecules 2020, 53, 2882-2892



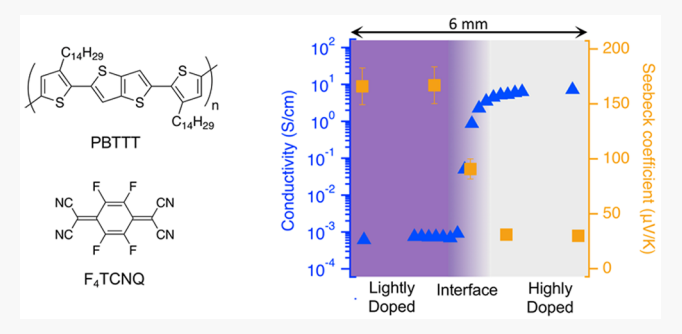
ACCESS

Metrics & More

Article Recommendations

s Supporting Information

ABSTRACT: With the ability to modulate electronic properties through molecular doping coupled with ease in processability, semiconducting polymers are at the forefront in enabling organic thermoelectric devices for thermal energy management. In contrast to uniform thermoelectric material properties, an alternative route focuses on functionally graded materials (FGMs) where one spatially controls and optimizes transport properties across the length of a thermoelectric material. While primarily studied in the context of inorganic materials, the concept of FGMs for organic thermoelectrics has not been explored. Herein, we introduce how molecular doping of semiconducting polymers enables spatial compositional control of thin-film FGMs. Specifically, we use



sequential vapor doping of poly[2,5-bis(3-tetradecylthiophen-2-yl)thieno[3,2-b]thiophene] (PBTTT) with the small molecule acceptor 2,3,5,6-tetrafluoro-7,7,8,8-tetracyanoquinodimethane (F4TCNQ) to fabricate the simplest form of FGMs—double-segmented thin films. The two thin-film segments are of equal length (7.5 mm) but each set to different doping levels. Our study focuses on understanding the thermoelectric properties (Seebeck coefficient, α , and electronic conductivity, σ) and structural properties (through X-ray scattering, UV—vis—NIR spectroscopy, and Raman spectroscopy) within and across the two segments. We observe the presence of a small diffuse interfacial region of 0.5–1 mm between the two segments where the doping level and transport properties vary continuously. Despite the diffuse interface, the measured α across the two segments is simply the average of α within each segment. Importantly, this experimental result is consistent with reported mathematical models describing the spatial average of α in graded thermoelectric materials. Our results demonstrate the facile fabrication and characterization of functionally graded organic thermoelectric materials, providing guidelines for further development on more complex FGMs.

■ INTRODUCTION

Molecular doping is an essential process in controlling charge carrier concentration and, in turn, the electronic transport properties of conjugated polymeric semiconductors. 1,2 Doped semiconducting polymers are of broad interesting spanning organic electronic and energy applications. 1,3 Recently, doped semiconducting polymers have emerged as promising materials for thermoelectrics—devices that interconvert heat and electricity.3-10 Polymers for thermoelectrics span poly-(ethylene dioxythiophene) (PEDOT), polythiophene derivatives (e.g., poly(2,5-bis(3-alkyl-2-thienyl)thieno[3,2-b]thiophene) [PBTTT] and poly(3-alkythiophene) [P3AT]), and more advanced polymers based on donor-acceptor conjugated moieties. Organic thermoelectrics based on these polymers can enable new device geometries and architectures that are challenging to achieve through traditional inorganicbased materials. By leveraging the processability of polymers, modules may be flexible and conformable. 11-13 In turn, unique designs, such as annular or corrugated modules, facilitate broader implementation toward waste heat harvesting, local temperature control (cooling), and low-power wearable electronics. $^{14-17}$

Fundamentally, challenges lie in controlling the highly interrelated material properties that dictate thermoelectric performance, which include electronic conductivity (σ) , Seebeck coefficient (or thermopower) (α) , and thermal conductivity (κ) . The thermal-to-electrical energy conversion efficiency is related to the dimensionless figure of merit, $ZT = \alpha^2 \sigma T/\kappa$, where T is the temperature in kelvin and $\alpha^2 \sigma$ is the power factor (PF). Unifying each transport property is the connection to the charge carrier concentration (n). In principle, the magnitude of σ increases as a function of n while, in contrast, the magnitude of α decreases with n. For the case of thiophene-based semiconducting polymers, the quantitative addition of a molecular p-dopant such as a small organic acceptor $(F4TCNQ_1, 2,3,5,6$ -tetrafluoro-7,7,8,8-

Received: February 19, 2020 Revised: March 25, 2020 Published: April 7, 2020





tetracyanoquinodimethane) leads to an electron transfer between the host polymer and dopant molecule, which modulates n. In addition, the introduction of the dopant must maintain the underlying hierarchical structure (crystalline order, orientation, and long-range morphology), enabling efficient charge transport in semiconducting polymers.

Therefore, how the dopant molecule is introduced into the polymer matrix is critical to controlling the thermoelectric material properties. 20,21 One approach includes casting films from solution mixtures of the polymer and dopant. While this process takes advantage of solution processability, controlling the morphology of films is difficult due to the formation of charged polymers, which results in significant aggregation or precipitation at high dopant loadings that leads to poor quality films.²² An alternative and most promising approach is the sequential doping method where one first casts a neat thin film, and then the dopant is infiltrated into the polymer matrix either with an orthogonal solvent or from the vapor phase.²²⁻²⁹ It has been shown that casting a thin film of PBTTT and then vapor doping with F4TCNQ leads to a thermoelectric PF around 120 μ W m⁻¹ K⁻², which is substantially higher relative to a film cast from a polymer/ dopant solution (1.3 μ W m⁻¹ K⁻²).²⁰ The high *PF* is achieved because the infiltration of the dopant into the polymer matrix maintains the crystalline order, orientation, and long-range chain connectivity permitting high charge carrier mobility. Applying a similar approach, a recent publication from Brinkmann and co-workers has shown that sequential doping of chain aligned PBTTT leads to a PF of about 2000 µW m K⁻²—a record for modern solution-processable semiconducting polymers.30

Inspired by facile processability of semiconducting polymers and the utility of the sequential doping process, we are exploring a new direction toward functionally graded forms of doped semiconducting polymers. Functionally graded materials (FGMs) are engineered materials where properties are varied spatially either continuously or a step-by-step (segmented) fashion throughout the volume of the material.31-33 Spatial control through composition, microstructure, and orientation can tune local properties across the FGM.³ Implementation of the functional grading principles offers an opportunity of increasing the efficiency of thermoelectric devices for power generation or cooling by employing appropriate distribution of n and microstructure.^{34–44} The effectiveness of FGMs has been exclusively investigated with inorganic thermoelectric materials (e.g., Bi₂Te₃ and PbTe).36,45,46 For perspective, a wide operating temperature range (up to ca. 1000 K) for power generation through inorganic materials leads to thermoelectric properties to be a strong function of temperature. 18 Therefore, tuning the dopant composition (carrier density) or microstructure across the operating temperature gradient permits local optimization of thermoelectric properties.³⁵ Alternatively, spatial variation of the thermoelectric properties enables more efficient distribution of heat when operating thermoelectrics as Peltier coolers.^{37,39} This design, termed the distributed Peltier effect, leads to larger cooling temperature gradients and coefficient of performance. Utilization of FGMs in the context of thermoelectric cooling applications (e.g., medical cooling devices, seat coolers, and thermal management for batteries) where the operating temperatures amenable to polymeric materials (e.g., ~60 to 0 °C) will be most promising for organic thermoelectrics.

To understand the influence of segmented to continuously graded thermoelectric properties, significant focus has been on developing mathematical models of FGMs based on first principles to establish the theoretical limits of performance. ^{37–39,42,47,48} These models provide experimental guiding principles for the fabrication and implementation of FGMs. However, the experimental synthesis and processing of conventional inorganic thermoelectric materials typically require high temperature (~1000 K) and pressure (50 MPa) conditions to produce ingots with appropriate gradient in dopant concentration or microstructure. Therefore, executing the principles of functional grading can be prohibitive due to extreme synthetic and processing conditions. In contrast, solution processability of semiconducting polymers and low temperature thermal processing conditions permits a deeper exploration of various forms of functionally graded motifs through a single material. In particular, gradient in microstructure can be achieved with solvent or thermal annealing while the sequential doping method enables spatial control of dopant composition. To best of our knowledge, the principles of functional grading have not been explored for organic thermoelectric materials.

To this end, we report on the fabrication, structure, and thermoelectric properties (σ and α) of symmetric doublesegmented thin films—the simplest form of a 1D functionally graded thin films. By design, the focus of the work is not motivated by device optimization but centered around a fundamental understanding of spatial structure-transport properties of molecularly doped semiconducting polymers through double-segmented thin films. We use the high mobility semiconducting polymer poly(2,5-bis(3-tetradecylthiophen-2-yl)thieno[3,2-b]thiophene) (PBTTT). The approach for this study employs compositional control of the molecular dopant F4TCNQ to modulate doping level (carrier concentration) within each macroscopic segment. Through a custom-designed vapor doping apparatus, we show how sequential vapor doping leads to facile fabrication of compositionally controlled double-segmented thin films. Through a combination of grazing incidence wide-angle Xray scattering (GIWAXS) and Raman spectroscopy, we characterize the local order and the lateral spatial distribution of the dopant within and across the boundary of the two segments. In addition, the spatial distribution of σ is measured through an array of microfabricated electrodes. The measurements reveal a more complex picture encompassing multiple forms of functional gradients across multiple length scales. In particular, the fabrication process leads to the formation of a diffuse interface at the boundary of two segments comprising a sigmoidal-like profile in doping and electronic conductivity. Lastly, the macroscopic α is measured within and between the segments to provide insight into the spatial average of α .

■ RESULTS AND DISCUSSION

Fabricating Double-Segmented Films through Sequential Vapor Doping. For facile fabrication of symmetric double-segmented PBTTT:F4TCNQ thin films, we employ sequential vapor doping to spatially control dopant composition in the lateral direction (Figure 1). It has been established that thin film processing controls the thermoelectric transport properties of molecular-doped semiconducting polymers like PBTTT. Therefore, for consistency, all neat PBTTT thin films are processed in the same manner in this study: spin-coated from chlorobenzene solution and soft annealed at 80 °C (as-

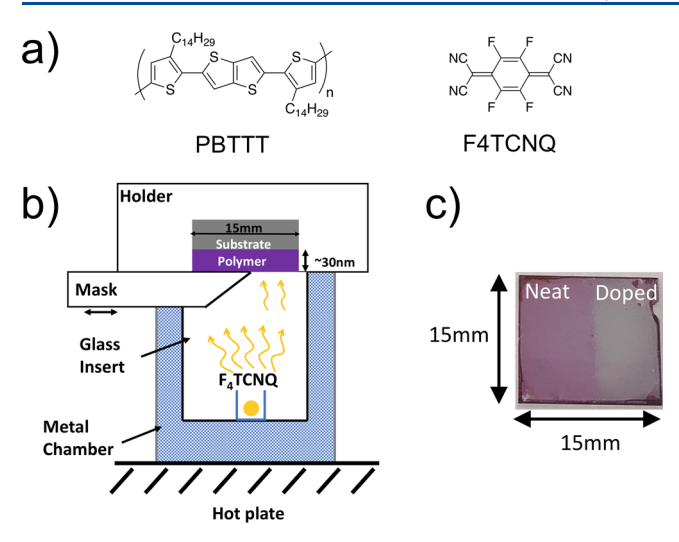


Figure 1. (a) Chemical structure of PBTTT and F4TCNQ. (b) Schematic of the fabrication process used in this study to achieve double-segmented PBTTT thin films. (c) Picture of a double-segmented thin film.

cast thin films of ca. 30 nm). By focusing on the thin film regime, we can ensure uniform composition of dopant through the thickness of the film (out-of-plane direction), and thus, spatial variation only occurs in the lateral direction (1D profile). In Figure 1b, we show a schematic of our home-built apparatus for controlled vapor doping of polymer thin films in an argon atmosphere glovebox. More details are provided in the Experimental Methods section and the Supporting Information. In short, a pellet of F4TCNQ in an alumina crucible is placed at the bottom of the doping chamber where the base is heated to $\sim\!200\,^{\circ}\text{C}$ to sublime F4TCNQ. The dopant vapor infiltrates a PBTTT thin film that has been placed in a Teflon holder at the top of the doping chamber. The extent of doping is controlled through vapor dopant exposure time.

We calibrated our doping chamber to determine the extent of doping and conductivity as a function of F4TCNO vapor exposure time. Figure 2a shows a semilog plot for the evolution of the four-probe electronic conductivity. We observe the typical superlinear increase in conductivity where the conductivity rapidly increases and then eventually plateaus at longer doping times. The values for conductivity are 0.10 S/cm at 1.5 min, 8 S/cm at 2 min, and 200 S/cm at 4 min. The corresponding UV-vis-NIR absorption spectra are shown in Figure 2b, indicating efficient charge transfer between PBTTT and F4TCNQ. For neat PBTTT, the primary absorption peak is observed at 2.3 eV and a broad shoulder at 2.1 eV. After vapor exposure, the absorption intensity of the primary peak decreases along with the appearance of absorption structure in the vicinity of 0.5 eV, corresponding to the positive polaron of PBTTT, and the appearance of peaks near 1.4 and 1.6 eV, corresponding to the radical anion of F4TCNQ.19 These absorption features are indicitive of the integer charge transfer doping mechanism.1

The doping levels in the films were estimated from deconvoluted UV–vis–NIR spectra using Beer's law (Figure S1). The F4TCNQ anion concentration was determined by using the F4TCNQ anion molar extinction coefficient at 1.4 eV ($\varepsilon \approx 50000~{\rm L~mol^{-1}~cm^{-1}}$),⁴⁹ and the underlying monomer concentration was estimated from the PBTTT extinction

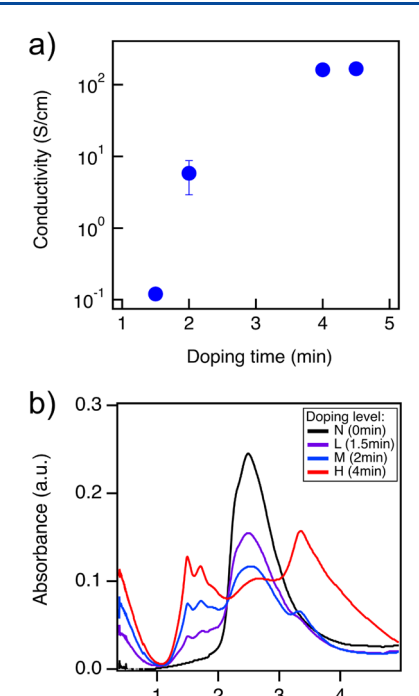


Figure 2. (a) Electronic conductivity of PBTTT thin films doped with F4TCNQ via the vapor doping method as a function of time. Conductivity of neat PBTTT was measured to be 1.5×10^{-5} S/cm. (b) UV-vis-NIR spectra of PBTTT thin films vapor-doped with F4TCNQ for various times. N = neat, L = low, M = medium, and H = high doping levels.

Energy (eV)

coefficient at 2.3 eV ($\varepsilon \approx 50000 \text{ L mol}^{-1} \text{ cm}^{-1}$) (see the Supporting Information for a detailed calculation). The estimated molar ratio (MR) of the dopant anion to monomer (F4TCNQ anion:PBTTT monomer) is 0.04, 0.09, and 0.23 for 1.5 min doped, 2 min doped, and 4 min doped films, respectively. The high doping level is approaching reported studies of PBTTT doped with F4TCNQ where the maximum MR is in the range of 0.25-0.30. With these results, we designate four doping and conductivity levels for our study: neat (undoped) (N), MR = 0.04 = low (L), MR = 0.09 = lowmedium (M), and MR = 0.23 = high (H). To generate segmented films, we used a Teflon bar to mask parts of the film from exposure to the dopant vapor (Figure 1b). More details are provided in the Experimental Methods section. Going forward, we will focus on the characterization of neat-high (NH), low-high (LH), and medium-high (MH) doublesegmented thin films.

Influence of Molecular Doping on Local Structure and Dopant Distribution. By performing grazing incidence wide-angle X-ray (GIWAXS) scattering experiments, we can determine how molecular doping influences the local ordering of the polymer chains and provides insight into the distribution of the dopant within and across the two segments. The GIWAXS images of our neat PBTTT thin film convey the characteristic scattering pattern for as-cast PBTTT (Figure S2). The GIWAXS image indicates side-chain stacking (h00) peaks up to the fourth order in the out-of-plane direction along with the backbone reflection $(\overline{113})$ as well as the reflection (110) related to the $\pi-\pi$ stacking in the in-plane direction. This observation indicates a preferential edge-

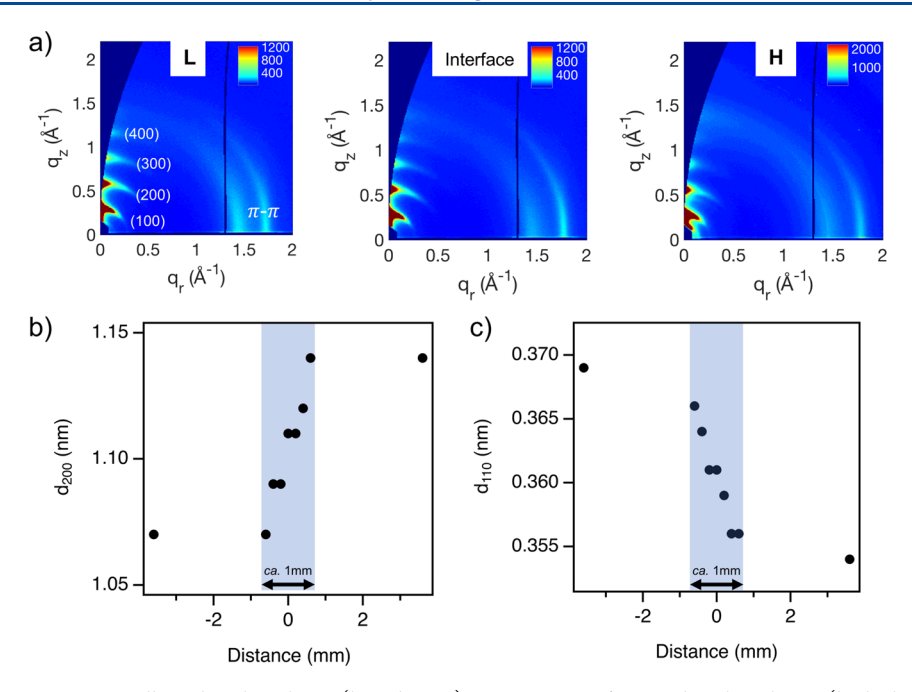


Figure 3. (a) 2D GIWAXS images collected within the L (low doping) segment, interface, and within the H (high doping) segment. Domain spacing of (b) (200) peak, d_{200} , and (c) (110) peak, d_{110} , at different positions on LH segmented thin films obtained from GIWAXS.

on orientation of polymer crystallites, resulting from the casting conditions used in this particular study.

For F4TCNQ-doped films, representative GIWAXS images are shown for the LH segmented film in Figure 3a and for the NH and MH segmented films in the Supporting Information (Figure S3). Overall, the scattering patterns for all segmented films are qualitatively similar to neat PBTTT. This indicates that vapor infiltration with F4TCNQ only causes minimal disruption to the underlying semicrystalline morphology of PBTTT, which is consistent with previous reports.²⁰ Quantitative changes upon vapor doping are seen through the side-chain stacking and π - π stacking distances. We focus on the (200) reflection to due to background scattering from the beamstop and substrate reflectivity present near the (100) reflection. In segment H, we observe an increase in the sidechain spacing distance (d_{200}) to 1.14 nm relative to 1.06 nm for neat PBTTT. In addition, we observe a compression of the π - π stacking distance to 0.354 nm relative to 0.371 nm for neat PBTTT.

These changes are consistent with recent reports showing that dopant F4TCNQ anion resides within regions of the aliphatic side chains where an expansion of the side-chain stacking direction (h00) and compression of the $\pi-\pi$ stacking distance are observed. The decrease in the $\pi-\pi$ stacking distance upon doping is widely observed in molecularly doped conjugated polymers. Recently, it has been shown that doping-induced polaron delocalization between adjacent backbones leads to electrostatically attractive intermolecular interactions and, thus, accounts for the reduction in the $\pi-\pi$ stacking distance. Moreover, the extent of the changes in the distances is a function of doping level. Therefore, we can use the relative changes in side-chain and $\pi-\pi$ stacking distances to monitor the compositional distribution of the dopant.

GIWAXS experiments as a function of angle of incidence were performed to determine the dopant composition through the thickness of the film (out-of-plane direction). In Figures S4 and S5, we show the scattering profiles measured at different

angles of incidence for segments L and H. Overall, the changes to side-chain stacking and $\pi-\pi$ stacking distances are the same at each angle of incidence, which signifies uniform distribution of dopant through the thickness of the film. These results are consistent with previous reports for PBTTT thin films used in this study (ca. 30 nm).²⁰

The lateral distribution of both side-chain stacking and $\pi-\pi$ stacking distances are shown in Figures 3b and 3c, respectively, for the LH segmented film and in the Supporting Information for NH and MH segmented films (Figures S6 and S7). Measurements were performed on nine different spots laterally across the double-segmented film (7.2 mm distance). The center location (x=0 mm) was designated as the location of edge of the Teflon bar during vapor doping, which defines the interface between the two segments. Seven measurements were conducted across the interface of the segments. The distance between adjacent spots is ~200 μ m, which is the width of the X-ray beam. Measurements within each segment were 3 mm away from the edge of the interface of the two segments.

Starting from within segment L (x = -3.6 mm), the secondorder side-chain spacing, d_{200} , is 1.07 nm and maintains this value when approaching the interface (x = -0.6 mm). Importantly, finer spatial measurements across the interface and toward segment H revealed a steady increase in d_{200} where the value reaches 1.14 nm at x = +0.6 mm. This d_{200} is equal to the value within segment H (x = +3.6 mm). The distribution can be qualitatively described to follow a sigmoidal-like profile. As shown in Figure 3c, the spatial distribution for $\pi - \pi$ stacking distance shows a similar sigmoidal profile, but inversely correlated. The profile reveals that while the doping level is homogeneous within each segment, there exists a thin diffuse interface where the doping level gradually changes. This distribution was also observed in NH and MH segmented films (Figures S6 and S7). Overall, the width of the diffuse interface is ca. 1 mm for NH and LH and ca. 0.5 mm for MH segmented films.

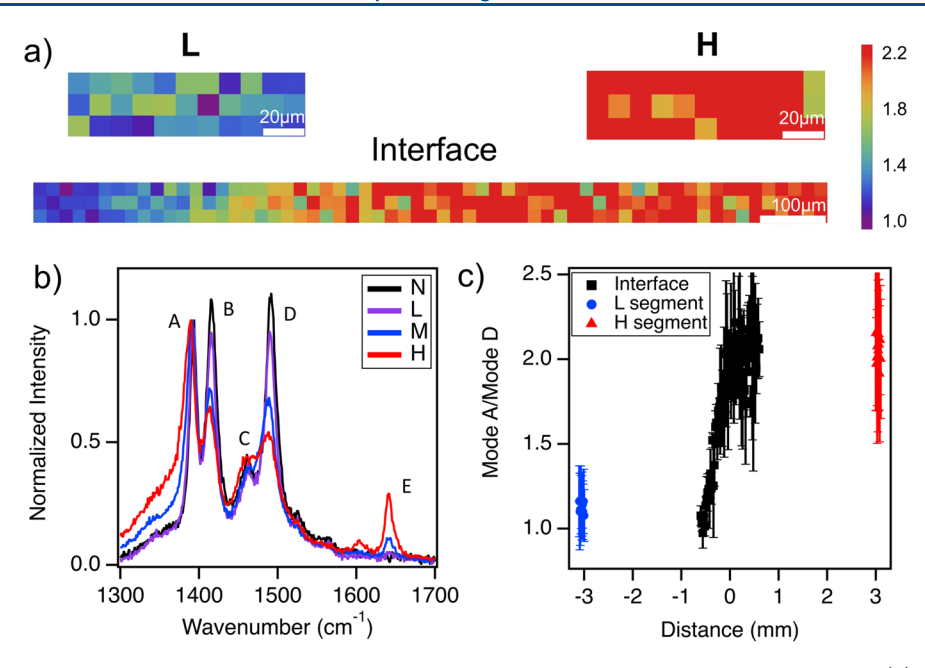


Figure 4. (a) Raman maps of peak height ratio of mode A/mode D on segment L, segment H, and across the interface. (b) Raman spectra for N, L, M, and H films with labeled Raman modes. (c) Peak height ratio of mode A/mode D as a function of distance across a LH segmented film. The Raman results for NH and MH segmented films are provided in the Supporting Information. N = neat, L = low, M = medium, and H = high doping levels.

Raman Spectroscopy Reveals Spatial Distribution of Charge Carriers. Raman spectroscopy was used to further characterize the spatial distribution of charge carriers (doping level) within and across the double-segmented PBTTT thin films. Charge carriers here correspond to the formation of positive polarons, which can be observed through changes in Raman vibrational modes of the conjugated core of PBTTT. Note that the determination of positive polarons through Raman spectroscopy is used to quantify the local doping level and should not be equated to be free charge carriers contributing to conduction.⁵⁶ Raman spectra of neat PBTTT and PBTTT:F4TCNQ thin films at various vapor doping times are shown in Figure 4b. For neat PBTTT, we observe four major Raman modes, appearing at 1394 cm⁻¹ (mode A), 1415 cm⁻¹ (mode B), 1460 cm⁻¹ (mode C), and 1490 cm⁻¹ (mode D). These modes are in good agreement with previous reports⁵⁷⁻⁵⁹ and are further summarized in Figure S8 and Table S1. The relevant modes to monitor polaron formation are A and D, which correspond to the C=C stretching mode from the thienothiophene core and the C=C/C-Cstretching/shrinking mode from the outer thiophene rings, respectively. 57-59 The relative intensity change of mode A indicates the formation of positive polarons (hole carriers) while the change to mode D relates to neutral (undoped) chains. In tandem, the appearance and growth of the peak at 1642 cm⁻¹ correspond to the formation of the F4TCNQ anion (mode E), which further emphasizes the correlation to the doping level. To best express relative changes between individual peak modes, we normalized all neat and doped Raman spectra to mode A. With this normalization scheme, the intensity of mode D is shown to decrease significantly upon doping with F4TCNQ. In turn, taking the peak height ratio of mode A/mode D approximates the positive polaron (hole) concentration. For example, the peak height ratio of mode A to mode D increases from 0.92 for neat PBTTT to 1.9 when PBTTT doped for 4 min. This relation provides us a pathway

to spatially map out the charge carrier concentration across key regions of the segmented film.

Figure 4a shows the Raman maps of peak height ratio of A/ D for different spots of the LH segmented film. Note that the spatial resolution of the Raman mapping is \sim 0.65 μ m based on the aperture of the microscope and laser wavelength. Moreover, each "pixel" of the color map is "coarse-grained" to a 10 μ m by 10 μ m square, which is based on the step size for each measurement. Here, purple corresponds to regions of lowest charge carrier concentration while red corresponds to regions of highest charge carrier concentration. Within segment H, we observe near uniform distribution of charge carriers. On the other hand, segment L shows a less homogeneous charge carrier distribution, suggesting dopant segregation at lower doping levels. Raman maps with finer scale (1 μ m step size) were also obtained to confirm this inhomogeneity (Figure S9). While doping level is uniform when macroscopically average, the Raman experiments show the inhomogeneity of doping at the submicrometer scale and, thus, the hierarchical nature of compositional dopant control inherent with the sequential vapor doing process.

The interfacial region between both segments, moreover, shows a gradual change in charge carrier concentration (Figure 4a and Figure S10). To quantify the width of the gradual change, we plot the lateral average of the ratio of modes A and D (Figure 4c and Figure S10b,d). The peak height ratio A/D is 1.1 ± 0.2 within segment L while the A/D ratio is 2.0 ± 0.4 within segment H. The large error arises from the heterogeneity of the charge carrier distribution. Across the interface region, the peak height ratio gradually increases from 1.0 (average of first three points) near segment L to 2.1 (average of last three points) near segment H. This gradual change describes a diffuse interface, which occurs across a width of ~ 1 mm for the LH segmented film. The presence of a diffuse interface is consistent with the analysis of the GIWAXS measurements discussed earlier.

Determination of Spatial Electronic Conductivity.

The spatial distribution of the electronic conductivity was characterized within and across the interface of the segments through an array of interdigitated electrodes (IDEs). Note that we designate the center IDE (x=0) as the spot where the edge of the Teflon mask was located during vapor doping, which establishes the boundary between the two segments. Each IDE measures a 100 μ m by 300 μ m region and is laterally spaced apart by 200 μ m, which yields a total distance of 6 mm (3 mm for each segment). Shown in Figure 5 is the spatial electronic

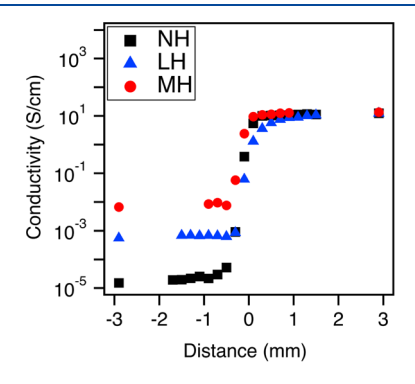


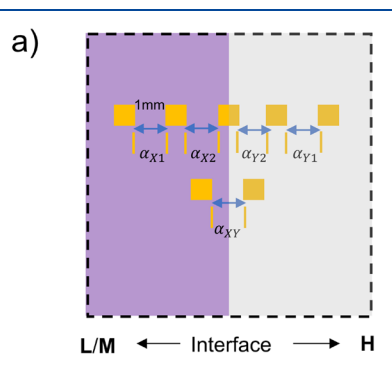
Figure 5. Electronic conductivity across the double-segmented films (measured by an array of IDEs, see the Supporting Information). The center spot (0 mm) is as the location where the edge of the Teflon mask was placed during vapor doping. N = neat, L = low, M = medium, and H = high doping levels.

conductivity for the three double-segmented thin films. The spatial distribution reveals uniform conductivity within each segment, but with the presence of a diffuse interface that has a sigmoidal-like conductivity profile. The width of the diffuse interface is dependent on the doping time and is ca. 1.5 mm for NH, ca. 1.0 mm for LH, and ca. 0.6 mm for MH segmented films. Importantly, the conductivity profile within the diffuse interface correlates well with the presence of a graded doping profile as observed through GIWAXS and Raman spectroscopy.

Description of Functional Gradient Forms in Our Double-Segmented Films. Conductivity, GIWAXS, and Raman experiments reveal that the fabrication of the doublesegmented film leads to a more intricate description encompassing multiple forms of functional grading across multiple length scales. Specifically, the description accounts for composition and structural characteristics spatially controlled from nano to macro scales. Our functionally graded films comprise macroscopic segments set to a specific doping level. As observed through Raman mapping, the dopant composition is heterogeneous in the submicrometer length scale. The heterogeneity and hierarchical dopant composition control the measured macroscopic electronic conductivity and Seebeck coefficient within each segment. Between the two segments is a diffuse interface where the dopant composition and conductivity vary continuously. Qualitatively, the functional grading profile of our double-segmented film can be described by a sigmoidal-like curve. The intricate nature of the functional gradient forms in our films will regulate the spatial average of the Seebeck coefficient (to be discussed in the next section). We posit the formation of the diffuse interface arises from the inhomogeneity of dopant infiltration from shadowing effects at edge of the bar and vapor diffusion underneath the microscopic gap between the bar and film surface. While

solid-state lateral drift diffusion can contribute to the diffuse interface, we believe this process is negligible in our experiments (see the Supporting Information, page S14). In total, these processes lead to a gradient in dopant concentration across the boundary of the two segments.

Determination of Macroscopic Seebeck Coefficient. In this section, we present and discuss the results for the measured macroscopic α values within and between the two segments. In Figure 6a, we show the geometry and



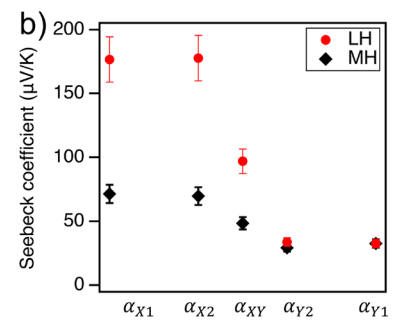


Figure 6. (a) Schematic of the contact geometry for spatial Seebeck coefficient measurements on LH and MH segmented films. (b) Seebeck coefficient at different regions of LH and MH segmented films (X = L or M; Y = H). N = neat, L = low, M = medium, and H = high doping levels.

arrangement of the gold contacts used to measure the Seebeck coefficient of the double-segmented films. The larger gold pads were used to measure the temperature difference while the narrow gold strips are used to measure the voltage difference. Measurements were taken each 1 mm apart to ensure sufficient voltage response. The Seebeck coefficient was spatially measured at five spots across the double-segmented film. The middle contact pair were for measurements between the interface of the two segments. Note that the distance of 1 mm is approximately similar to or larger than the width of the diffuse interface. In addition, the location of the metal contacts was controlled so that measurement equally weights each segment when measuring across the interface.

Measurements within segments L and H yielded values of $\alpha_{L1}=177\pm17~\mu V/K$ and $\alpha_{L2}=178\pm17~\mu V/K$ and $\alpha_{H1}=33\pm3~\mu V/K$ and $\alpha_{H2}=34\pm3~\mu V/K$. In addition, the MH segmented film yielded values of $\alpha_{M1}=71\pm7~\mu V/K$ and $\alpha_{M2}=70\pm7~\mu V/K$ and $\alpha_{H1}=33\pm3~\mu V/K$ and $\alpha_{H2}=30\pm3~\mu V/K$. Overall, these values reveal the homogeneity of the macroscopic Seebeck coefficient within each segment. The measurement of α across the segments yielded values of $\alpha_{LH}=97\pm9~\mu V/K$ and $\alpha_{MH}=48\pm5~\mu V/K$ for the two segmented films. Upon closer inspection, α_{LH} and α_{MH} are the average of

the α values of each corresponding homogeneous segment (Figure 6b). This observation holds true when α is measured along a longer distance of 3 mm across the two segments (Figure S11).

This averaging effect can be validated by considering the general integral expression for the spatial average (α_{avg}) for a graded α profile:

$$\alpha_{\text{avg}} = \frac{1}{L} \int_0^L \alpha(x) \, dx \tag{1}$$

where $\alpha(x)$ is the spatial distribution function of the graded Seebeck coefficient and L is the total lateral distance of the graded profile.³⁵ For our symmetric double-segmented films, the integration can be simplified as the sum of the rectangular integration of each segment $(\alpha_1L_1 + \alpha_2L_2)$. Dividing by the total length $(L = L_1 + L_2)$ leads to the average Seebeck coefficient. Note our double-segmented films are symmetric so $L_1 = L_2$; therefore, eq 1 simplifies down to $(\alpha_1 + \alpha_2)/2$, or the average of each homogeneous segment. Indeed, α_{LH} is measured to be 97 \pm 9 μ V/K, which is the same as the integrated average, 105 \pm 10 μ V/K, within error. Similarly, for the MH segmented film, the integrated average is 51 \pm 5 μ V/K, which is equivalent to the measured $\alpha_{MH} = 48 \pm 5 \ \mu$ V/K.

The above analysis does not account for the small diffuse interface between the two segments where the doping level has a sigmoidal-like profile. While we could not experimentally map out the local Seebeck coefficient, it can be reasonably assumed the spatial distribution for α inversely correlates to the dopant composition and conductivity profiles shown earlier. For discussion purposes, we calculated the spatial α profile using the experimental spatial conductivity (Figure 5) and the empirical power law correlation previously reported for polythiophene-based polymers (α proportional to $\sigma^{-1/4}$, Figure S12). The calculated local α spatial profile for the segmented films is shown in Figure S13. With a nearly symmetric sigmoidal-like profile, the average of the two asymptotic values corresponds to the inflection point of the curve. As noted earlier, the experimental measurement distance of 1 mm for α is approximately similar to or larger than the width of the diffuse interface. Consequently, the Au Seebeck contacts reside on the asymptotes of the sigmoidal-like profile where the asymptotes track each homogeneous segment. By design, the experimental α measurement equally balances each segment; thus, the measured α across the segment is equivalent to the local α at the midpoint point (inflection point) within the diffuse interface. Therefore, because of the symmetry of the α profile and equal weighting of each segment, the spatial distribution of α within the diffuse interface does not impact the determination of the average Seebeck coefficient of our double-segmented films.

CONCLUSIONS

We have presented a facile process in fabricating symmetric double-segmented PBTTT thin films where each segment is sequentially doped with F4TCNQ from the vapor phase. To characterize the lateral dopant composition profile, we correlated the changes in the characteristic side-chain stacking and $\pi-\pi$ stacking distances to the presence of dopant anion molecules. While uniform side-chain stacking and $\pi-\pi$ stacking distance were seen within each segment (uniform doping level), a gradual change in these characteristic spacings was seen across the interface of the segments (gradient in doping level). Of note, the length of this diffuse interface is

0.5–1 mm between the two segments. In addition, Raman spectroscopy provided complementary details in the localized doping level. While Raman mapping revealed inhomogeneity of doping at the submicrometer scale, the macroscopic average of the spatial doping profile follows the trends observed with GIWAXS. Spatial conductivity measurements through an array of microelectrodes indicated sigmoidal-like profile tracking well with the dopant compositional profile. Lastly, the Seebeck coefficient (α) was measured within and the across the segments. The measurements revealed homogeneity of the macroscopic Seebeck coefficient within each segment. Even with presence of the diffuse interface, the spatiality integrated α was simply the average of the α values of the segments.

Our work showcases how sequential vapor doping is an enabling technique for applying the principles of functional grading for organic thermoelectrics. While this study is limited to symmetric double-segmented films, going forward, more complex designs spanning multisegments to continuously graded profiles are possible. Moreover, for judicious selection of graded profiles, the design process can be coupled with mathematical transport models revealing theoretical limits of thermoelectric performance. Overall, semiconducting polymers as FGMs are an enabling platform to further advance our understanding of structure-transport properties and the development of more efficient organic thermoelectric devices.

EXPERIMENTAL METHODS

Materials. Poly(2,5-bis(3-tetradecylthiophen-2-yl)thieno[3,2-b]-thiophene) (PBTTT) and anhydrous chlorobenzene (CB) were purchased from Sigma-Aldrich ($M_{\rm w}$ 40000–80000) and used as received without further purification. 2,3,5,6-Tetrafluoro-7,7,8,8-tetracyanoquinodimethane (F4TCNQ₁ >98%) was purchased from TCI Chemicals.

Thin Film Preparation. Thin film samples for GIWAXS experiments were prepared on silicon with native oxide wafer substrates (15 mm × 15 mm × 0.5 mm, University Wafer). Thin film samples for UV-vis-NIR spectroscopy, Raman spectroscopy, and electrical characterization were prepared on quartz substrates (15 mm × 15 mm × 0.5 mm, University Wafer). All substrates were cleaned by sonicating in acetone and isopropanol for 10 min each, followed by plasma cleaning for 3 min. For neat PBTTT thin film preparation, PBTTT was dissolved in anhydrous CB (10 mg/mL), and the solution was heated at 80 °C for 2 h to fully dissolve the polymer. Then thin films were spin-coated by a SCS G3P spin-coater from the heated solution (80 °C) using a two-step spin condition of 2000 rpm for 40 s followed by 3000 rpm for 25 s. Films were heated at 80 °C for 10 min to remove residual solvent. All solution preparation, spin-coating, and drying steps were performed in an argon glovebox. The thickness of neat films was measured via ellipsometry, which was determined to be ≈30 nm.

Vapor Doping Process. Vapor doping was performed in an argon glovebox. Approximately 2 mg of F4TCNQ powder was pressed into a pellet (\sim 3 mm in diameter) and placed in an aluminum oxide crucible (OD 6.8 mm × H 4 mm from Government Scientific Source Inc.), which was in turn placed in a glass insert (diameter \sim 5 cm, height \sim 4.5 cm). A stainless-steel container was then preheated for 30 min on a hot plate to allow the chamber to reach a steady temperature at 200 °C (measured via a thermocouple at the base of the chamber). The glass insert with the dopant inside was put into the metal chamber to produce dopant vapor. For uniform doping of films (unsegmented films), a neat PBTTT thin film was held in a Teflon holder and placed on the top of the doping chamber. The doping level was controlled as a function of dopant exposure time. For this study, we define four doping levels: neat (N, 0 min), low (L, \sim 1.5 min), medium (M, \sim 2 min), and high (H, \sim 4 min) (Figure 2).

Double-segmented films were fabricated through a sequential vapor doping process. First, the whole polymer film was exposed to

F4TCNQ vapor to achieve L doping level or M doping level. Second, the Teflon holder being was removed from the chamber, and a Teflon bar (see dimensions in Figure S14) was then used as a mask to cover half of the film. Then, the holder was put back onto the chamber to further expose the uncovered half of the film to F4TCNQ vapor. For the film at L doping level, the film was exposed to F4TCNQ vapor for an additional 3 min to achieve an LH segmented film. For the film at M doping level, the film was exposed to F4TCNQ vapor for an additional 2 min to achieve a MH segmented film. Starting with a neat film, the film was exposed to F4TCNQ vapor for 4 min to achieve an NH segmented film.

UV-Vis-NIR. UV-vis-NIR spectra of neat PBTTT and vapordoped thin films on quartz substrates were obtained by using the Shimadzu UV-3600 Plus UV-vis-NIR dual beam spectrophotometer housed in the Soft Matter Characterization Facility (SMCF) (Pritzker School of Molecular Engineering, University of Chicago). Measurements were taken within a wavelength range of 300–3300 nm.

Grazing Incidence Wide-Angle X-ray Diffraction. GIWAXS experiments were conducted at the Advanced Photon Source (Argonne National Laboratory) at beamline 8-ID-E. The energy of the incident beam was at 10.91 keV, and scattering images were collected using a Pilatus 1MF pixel array detector (pixel size = 172 μ m). The measurement time for one image was 10 s. All samples were placed and measured in a low-vacuum chamber (10⁻³ mbar) to reduce the air scattering as well as to minimize beam radiation damage. There are multiple rows of inactive pixels between the detector modules when the images were collected at one position. To fill these inactive gaps, the detector was moved down to a preset new position along the vertical direction after each measurement. After the image was collected at the new spot, the data from these two detector positions were combined by using the GIXSGUI package for MATLAB to fill the inactive gaps. 61 The absence of artifacts in the combined image demonstrates that the scattering from the sample does not change during the exposure. The GIXSGUI package was also used to output the GIWAXS signals as intensity maps in (q_r, q_z) space and take the linecuts along out-of-plane (q_z) and in-plane directions

GIWAXS images of segmented thin films were taken at a grazing incident X-ray angle of 0.14° , which is above the critical angle of the polymer film surface and below the critical angle of the silicon substrate. GIWAXS images measured laterally across nine different spots for the double-segmented films. One measurement within each segment were 3 mm away from the interface of the segmented film. The other seven measurements were conducted laterally across the interface of the segmented films. The distance between adjacent spots is $200~\mu\text{m}$, which is the width of the X-ray beam. Lastly, for the depth-dependent experiments on doped PBTTT thin films, images were taken across a range of incidence angles $(0.08^\circ, 0.10^\circ, 0.12^\circ, 0.14^\circ, 0.16^\circ, 0.18^\circ, \text{ and } 0.20^\circ)$ to obtain scattering from the surface, bulk, and the polymer/substrate interface of doped PBTTT thin films (Figures S4 and S5).

Raman Spectroscopy. Raman spectroscopy experiments were performed under ambient conditions using the Horiba LabRAM HR Evolution NIR confocal Raman microscope housed in Chicago Materials Research Center. Raman spectra of neat and doped PBTTT thin films was collected by using a 100× objective and a 532 nm wavelength laser. The Raman spectra on segmented thin films were collected by using a 50× objective and the same 532 nm wavelength laser. The spatial resolution of each measurement is dependent on the numerical aperture of the microscope objective, the wavelength of the laser used, and the pinhole size of the confocal imaging mode. In our configuration, the spatial resolution of each Raman spectra is calculated to be 0.65 μ m. The laser power and accumulation time were set to 1% and 10 s to minimize local heating and material degradation. Spatial Raman spectra within each segment were acquired by using a step size of 10 μ m for a 100 μ m \times 100 μ m region or using a step size of 1 μ m for a 10 μ m \times 10 μ m region for finer measurements. Spatial Raman spectra across the interface of the two segments were acquired by using a step size of 10 μm for the $1000 \ \mu m \times 20 \ \mu m$ region. The time to collect a Raman map of 100

 $\mu m \times 100~\mu m$ is about 5–6 min. This minimized possible degradations that occurred during the measurement.

To generate a Raman color map, the ratio of peak intensity of mode A (representing the C=C stretching mode on the thienothiophene core) and mode D (representing the C=C stretching localized on the thiophene rings) was recorded for every Raman spectrum. The recorded ratios were autosaved in text file by the software and then exported into Wolfram Mathematica to plot as color maps. The color scale for every Raman map followed a rainbow color scheme where purple represents neat (ratio = 0.9) and red represents highly doped (ratio = 2.2).

Conductivity and Seebeck Measurements. Gold electrical contacts (75 nm thick) for electronic conductivity (σ) and Seebeck coefficient (α) measurements were deposited onto either uniform or segmented PBTTT thin films via thermal evaporation through shadow masks designed in our lab. The electronic conductivity was measured in the in-plane direction by using four probe geometry with a 0.2 mm spacing between electrodes and electrodes length of 1 mm. The Seebeck coefficient was measured with two 1 mm² gold pads, which are either 3 or 1 mm apart. A detailed schematic is provided in Figure S15. Four probe conductivity measurements were performed using a custom-designed probe station in an argon glovebox. Voltage and current measurements were performed using a Keithley 2400 source meter and a Keithley 6221 precision current source. A constant current was applied to the outer contacts, and the resultant steadystate voltage response was recorded from the two inner contacts. The resistance (R; ohm) of the sample was extracted from the slope of the $\it IV$ sweep by using Ohm's law ($\it V=\it IR$). The thin film conductivity σ was then calculated via the following equation:

$$\sigma = \frac{\ln 2}{\pi h R}$$

where h = 30 nm is the thickness of the sample.

The Seebeck coefficient measurements were performed on the same probe station. Two Peltier elements were placed 5 mm apart to provide the temperature difference ($\Delta T = T_{\rm H} - T_{\rm C}$). Two thermocouples were used to collect the hot and cold side temperatures, and two probes were used to measure the corresponding voltage value. A minimal amount of thermally conductive silicone paste was applied to the tips of the thermocouple to ensure good thermal contact between the thermocouple and the gold pads. A delay of 200 s was used for voltage measurements to ensure that a steady-state temperature gradient and voltage were reached. The Seebeck coefficient was calculated from the slope of a linear fit for the ΔV vs ΔT plot. A representative plot can be found in Figure S16. The measurements were taken within an approximate ΔT of ±3 K around 300 K so that the Seebeck coefficient did not change significantly over $T \pm \Delta T$. A series of measurements on nickel foil (0.03 mm, >99.9%) were performed at 25 °C to determine the systematic error (Figure S17). The measured Seebeck coefficient of Ni is $-20.3 \pm 1.3 \,\mu\text{V/K}$, which matched with reported values in the literature $(-19 \mu V/K \text{ at } 25 \text{ }^{\circ}C)$.

The spatial measurements of the electronic conductivity were performed using an array of interdigitated electrodes (IDEs). Interdigitated electrode devices were fabricated at the Pritzker Nanofabrication Facility, University of Chicago (see detailed fabrication process in the Supporting Information and Figure S18). The measurements were performed using the DC measurement method. The extracted resistance R was then used to calculate the electronic conductivity $\sigma_{\rm IDE}$ according to the following equation:

$$\sigma_{\text{IDE}} = \frac{1}{R} \frac{d}{l(N-1)h}$$

Here, $d=8 \mu \text{m}$ is the separation distance between electrodes, $l=100 \mu \text{m}$ is the electrode length, N=40 is the number of electrodes, and h=30 nm is the thickness of the film.

ASSOCIATED CONTENT

Supporting Information

The Supporting Information is available free of charge at https://pubs.acs.org/doi/10.1021/acs.macromol.0c00402.

Determination of doping level, 2D GIWAXS images for neat, NH, MH segmented films, GIWAXS depth profiling, 1D scattering curves, domain spacing profile for segmented films, Raman spectra and mode assignments, Raman mapping profiles of segmented films, conductivity and Seebeck data, experimental details for Seebeck measurements, and IDE fabrication (PDF)

AUTHOR INFORMATION

Corresponding Author

Shrayesh N. Patel — Pritzker School of Molecular Engineering, University of Chicago, Chicago, Illinois 60637, United States; Center for Molecular Engineering, Argonne National Laboratory, Lemont, Illinois 60439, United States;

orcid.org/0000-0003-3657-827X; Email: shrayesh@uchicago.edu

Authors

Tengzhou Ma — Pritzker School of Molecular Engineering, University of Chicago, Chicago, Illinois 60637, United States; orcid.org/0000-0002-9116-5518

Ban Xuan Dong — Pritzker School of Molecular Engineering, University of Chicago, Chicago, Illinois 60637, United States; occid.org/0000-0002-2873-5207

Garrett L. Grocke — Pritzker School of Molecular Engineering, University of Chicago, Chicago, Illinois 60637, United States; orcid.org/0000-0001-8661-5038

Joseph Strzalka — X-ray Science Division, Argonne National Laboratory, Lemont, Illinois 60439, United States;
orcid.org/0000-0003-4619-8932

Complete contact information is available at: https://pubs.acs.org/10.1021/acs.macromol.0c00402

Notes

The authors declare no competing financial interest.

ACKNOWLEDGMENTS

This work was primarily supported by the University of Chicago Materials Research Science and Engineering Center, which is funded by National Science Foundation under Award DMR-1420709. B.X.D. was supported by NSF DMREF Award 1922259. This research used resources of the Advanced Photon Source, an Office of Science User Facility operated for the U.S. Department of Energy (DOE) by Argonne National Laboratory under Contract DE-AC02-06CH11357. Parts of this work were performed at the Soft Matter Characterization Facility of the University of Chicago. This work made use of the Pritzker Nanofabrication Facility of the Pritzker School of Molecular Engineering at the University of Chicago, which receives support from Soft and Hybrid Nanotechnology Experimental (SHyNE) Resource (NSF ECCS-1542205), a node of the National Science Foundation's National Nanotechnology Coordinated Infrastructure.

REFERENCES

(1) Salzmann, I.; Heimel, G.; Oehzelt, M.; Winkler, S.; Koch, N. Molecular Electrical Doping of Organic Semiconductors: Fundamen-

- tal Mechanisms and Emerging Dopant Design Rules. Acc. Chem. Res. 2016, 49 (3), 370–378.
- (2) Jacobs, I. E.; Moulé, A. J. Controlling Molecular Doping in Organic Semiconductors. *Adv. Mater.* **2017**, *29* (42), 1703063.
- (3) Glaudell, A. M.; Cochran, J. E.; Patel, S. N.; Chabinyc, M. L. Impact of the Doping Method on Conductivity and Thermopower in Semiconducting Polythiophenes. *Adv. Energy Mater.* **2015**, *5* (4), 1401072.
- (4) Kroon, R.; Mengistie, D. A.; Kiefer, D.; Hynynen, J.; Ryan, J. D.; Yu, L.; Müller, C. Thermoelectric Plastics: From Design to Synthesis, Processing and Structure-Property Relationships. *Chem. Soc. Rev.* **2016**, 45 (22), 6147–6164.
- (5) Zhang, Q.; Sun, Y.; Xu, W.; Zhu, D. What To Expect from Conducting Polymers on the Playground of Thermoelectricity: Lessons Learned from Four High-Mobility Polymeric Semiconductors. *Macromolecules* **2014**, *47* (2), 609–615.
- (6) Guo, J.; Li, G.; Reith, H.; Jiang, L.; Wang, M.; Li, Y.; Wang, X.; Zeng, Z.; Zhao, H.; Lu, X.; Schierning, G.; Nielsch, K.; Liao, L.; Hu, Y. Doping High-Mobility Donor-Acceptor Copolymer Semiconductors with an Organic Salt for High-Performance Thermoelectric Materials. *Adv. Electron. Mater.* **2020**, *6* (3), 1900945.
- (7) Liu, J.; Garman, M. P.; Dong, J.; van der Zee, B.; Qiu, L.; Portale, G.; Hummelen, J. C.; Koster, L. J. A. Doping Engineering Enables Highly Conductive and Thermally Stable N-Type Organic Thermoelectrics with High Power Factor. ACS Appl. Energy Mater. 2019, 2 (9), 6664–6671.
- (8) Untilova, V.; Biskup, T.; Biniek, L.; Vijayakumar, V.; Brinkmann, M. Control of Chain Alignment and Crystallization Helps Enhance Charge Conductivities and Thermoelectric Power Factors in Sequentially Doped P3HT:F4TCNQ Films. *Macromolecules* **2020**..
- (9) Serrano-Claumarchirant, J. F.; Culebras, M.; Muñoz-Espí, R.; Cantarero, A.; Gómez, C. M.; Collins, M. N. PEDOT Thin Films with N-Type Thermopower. *ACS Appl. Energy Mater.* **2020**, 3 (1), 861–867.
- (10) Lu, Y.; Wang, J.-Y.; Pei, J. Strategies To Enhance the Conductivity of N-Type Polymer Thermoelectric Materials. *Chem. Mater.* **2019**, *31* (17), 6412–6423.
- (11) Russ, B.; Glaudell, A.; Urban, J. J.; Chabinyc, M. L.; Segalman, R. A. Organic Thermoelectric Materials for Energy Harvesting and Temperature Control. *Nat. Rev. Mater.* **2016**, *1* (10), 16050.
- (12) Bahk, J.-H.; Fang, H.; Yazawa, K.; Shakouri, A. Flexible Thermoelectric Materials and Device Optimization for Wearable Energy Harvesting. *J. Mater. Chem. C* **2015**, 3 (40), 10362–10374.
- (13) Chen, Y.; Zhao, Y.; Liang, Z. Solution Processed Organic Thermoelectrics: Towards Flexible Thermoelectric Modules. *Energy Environ. Sci.* **2015**, 8 (2), 401–422.
- (14) Fang, H.; Popere, B. C.; Thomas, E. M.; Mai, C.-K.; Chang, W. B.; Bazan, G. C.; Chabinyc, M. L.; Segalman, R. A. Large-Scale Integration of Flexible Materials into Rolled and Corrugated Thermoelectric Modules. *J. Appl. Polym. Sci.* 2017, 134 (3), 44208.
- (15) Ryan, J. D.; Mengistie, D. A.; Gabrielsson, R.; Lund, A.; Müller, C. Machine-Washable PEDOT:PSS Dyed Silk Yarns for Electronic Textiles. *ACS Appl. Mater. Interfaces* **2017**, *9* (10), 9045–9050.
- (16) Elmoughni, H. M.; Menon, A. K.; Wolfe, R. M. W.; Yee, S. K. A Textile-Integrated Polymer Thermoelectric Generator for Body Heat Harvesting. *Adv. Mater. Technol.* **2019**, *4* (7), 1800708.
- (17) Jin, W.; Liu, L.; Yang, T.; Shen, H.; Zhu, J.; Xu, W.; Li, S.; Li, Q.; Chi, L.; Di, C.; Zhu, D. Exploring Peltier Effect in Organic Thermoelectric Films. *Nat. Commun.* **2018**, 9 (1), 3586.
- (18) Snyder, G. J.; Toberer, E. S. Complex Thermoelectric Materials. *Nat. Mater.* **2008**, 7 (2), 105–114.
- (19) Cochran, J. E.; Junk, M. J. N.; Glaudell, A. M.; Miller, P. L.; Cowart, J. S.; Toney, M. F.; Hawker, C. J.; Chmelka, B. F.; Chabinyc, M. L. Molecular Interactions and Ordering in Electrically Doped Polymers: Blends of PBTTT and F 4 TCNQ. *Macromolecules* **2014**, 47 (19), 6836–6846.
- (20) Patel, S. N.; Glaudell, A. M.; Peterson, K. A.; Thomas, E. M.; O'Hara, K. A.; Lim, E.; Chabinyc, M. L. Morphology Controls the

- Thermoelectric Power Factor of a Doped Semiconducting Polymer. Sci. Adv. 2017, 3 (6), No. e1700434.
- (21) Lim, E.; Glaudell, A. M.; Miller, R.; Chabinyc, M. L. The Role of Ordering on the Thermoelectric Properties of Blends of Regioregular and Regiorandom Poly(3-hexylthiophene). *Adv. Electron. Mater.* **2019**, *5*, 1800915.
- (22) Scholes, D. T.; Hawks, S. A.; Yee, P. Y.; Wu, H.; Lindemuth, J. R.; Tolbert, S. H.; Schwartz, B. J. Overcoming Film Quality Issues for Conjugated Polymers Doped with F4TCNQ by Solution Sequential Processing: Hall Effect, Structural, and Optical Measurements. *J. Phys. Chem. Lett.* **2015**, *6* (23), 4786–4793.
- (23) Jacobs, I. E.; Aasen, E. W.; Oliveira, J. L.; Fonseca, T. N.; Roehling, J. D.; Li, J.; Zhang, G.; Augustine, M. P.; Mascal, M.; Moulé, A. J. Comparison of Solution-Mixed and Sequentially Processed P3HT:F4TCNQ Films: Effect of Doping-Induced Aggregation on Film Morphology. J. Mater. Chem. C 2016, 4 (16), 3454–3466.
- (24) Patel, S. N.; Glaudell, A. M.; Kiefer, D.; Chabinyc, M. L. Increasing the Thermoelectric Power Factor of a Semiconducting Polymer by Doping from the Vapor Phase. *ACS Macro Lett.* **2016**, *S* (3), 268.
- (25) Hynynen, J.; Kiefer, D.; Yu, L.; Kroon, R.; Munir, R.; Amassian, A.; Kemerink, M.; Müller, C. Enhanced Electrical Conductivity of Molecularly P-Doped Poly(3-Hexylthiophene) through Understanding the Correlation with Solid-State Order. *Macromolecules* **2017**, *50* (20), 8140–8148.
- (26) Lim, E.; Peterson, K. A.; Su, G. M.; Chabinyc, M. L. Thermoelectric Properties of Poly(3-Hexylthiophene) (P3HT) Doped with 2,3,5,6-Tetrafluoro-7,7,8,8-Tetracyanoquinodimethane (F4TCNQ) by Vapor-Phase Infiltration. *Chem. Mater.* **2018**, 30 (3), 998–1010.
- (27) Kang, K.; Watanabe, S.; Broch, K.; Sepe, A.; Brown, A.; Nasrallah, I.; Nikolka, M.; Fei, Z.; Heeney, M.; Matsumoto, D.; Marumoto, K.; Tanaka, H.; Kuroda, S.; Sirringhaus, H. 2D Coherent Charge Transport in Highly Ordered Conducting Polymers Doped by Solid State Diffusion. *Nat. Mater.* **2016**, *15* (8), 896–902.
- (28) Hamidi-Sakr, A.; Biniek, L.; Bantignies, J.-L.; Maurin, D.; Herrmann, L.; Leclerc, N.; Lévêque, P.; Vijayakumar, V.; Zimmermann, N.; Brinkmann, M. A Versatile Method to Fabricate Highly In-Plane Aligned Conducting Polymer Films with Anisotropic Charge Transport and Thermoelectric Properties: The Key Role of Alkyl Side Chain Layers on the Doping Mechanism. *Adv. Funct. Mater.* **2017**, 27 (25), 1700173.
- (29) Vijayakumar, V.; Zaborova, E.; Biniek, L.; Zeng, H.; Herrmann, L.; Carvalho, A.; Boyron, O.; Leclerc, N.; Brinkmann, M. Effect of Alkyl Side Chain Length on Doping Kinetics, Thermopower, and Charge Transport Properties in Highly Oriented F4TCNQ-Doped PBTTT Films. ACS Appl. Mater. Interfaces 2019, 11 (5), 4942–4953.
- (30) Vijayakumar, V.; Zhong, Y.; Untilova, V.; Bahri, M.; Herrmann, L.; Biniek, L.; Leclerc, N.; Brinkmann, M. Bringing Conducting Polymers to High Order: Toward Conductivities beyond 10 5 S Cm –1 and Thermoelectric Power Factors of 2 MW m –1 K –2. *Adv. Energy Mater.* **2019**, *9*, 1900266.
- (31) Liu, Z.; Meyers, M. A.; Zhang, Z.; Ritchie, R. O. Functional Gradients and Heterogeneities in Biological Materials: Design Principles, Functions, and Bioinspired Applications. *Prog. Mater. Sci.* **2017**, *88*, 467–498.
- (32) Müller, E.; Drašar, Č.; Schilz, J.; Kaysser, W. A. Functionally Graded Materials for Sensor and Energy Applications. *Mater. Sci. Eng.*, A 2003, 362, 17.
- (33) Almasi, D.; Sadeghi, M.; Lau, W. J.; Roozbahani, F.; Iqbal, N. Functionally Graded Polymeric Materials: A Brif Review of Current Fabrication Methods and Introduction of a Novel Fabrication Method. *Mater. Sci. Eng., C* **2016**, *64*, 102–107.
- (34) Kuznetsov, V. L.; Kuznetsova, L. A.; Kaliazin, A. E.; Rowe, D. M. High Performance Functionally Graded and Segmented Bi2Te3-Based Materials for Thermoelectric Power Generation. *J. Mater. Sci.* **2002**, *37* (14), 2893–2897.

- (35) Müller, E.; Zabrocki, K.; Goupil, C.; Snyder, G. J.; Seifert, W. Functionally Graded Thermoelectric Generator and Cooler Elements. In *Materials, Preparation, and Characterization in Thermoelectrics*; Rowe, D. M., Ed., CRC Press: 2017; pp 46–81.
- (36) Hedegaard, E. M. J.; Mamakhel, A. A. H.; Reardon, H.; Iversen, B. B. Functionally Graded (PbTe) 1- x (SnTe) x Thermoelectrics. *Chem. Mater.* **2018**, 30 (1), 280–287.
- (37) Müller, E.; Walczak, S.; Seifert, W. Optimization Strategies for Segmented Peltier Coolers. *Phys. Status Solidi A* **2006**, 203 (8), 2128–2141.
- (38) Bian, Z.; Wang, H.; Zhou, Q.; Shakouri, A. Maximum Cooling Temperature and Uniform Efficiency Criterion for Inhomogeneous Thermoelectric Materials. *Phys. Rev. B: Condens. Matter Mater. Phys.* **2007**, 75 (24), 1–7.
- (39) Bian, Z.; Shakouri, A. Cooling Enhancement Using Inhomogeneous Thermoelectric Materials. In 2006 25th International Conference on Thermoelectrics; IEEE: 2006; pp 264–267.
- (40) Belov, I. M.; Volkov, V. P.; Manyakin, O. Optimization of Peltier Thermocouple Using Distributed Peltier Effect. *Thermoelectr.* 1999. Eighteenth Int. Conf. 1999, No. 095, 316–318.
- (41) Kim, C.; Kim, D. H.; Kim, J. S.; Han, Y. S.; Chung, J. S.; Kim, H. A Study of the Synthesis of Bismuth Tellurium Selenide Nanocompounds and Procedures for Improving Their Thermoelectric Performance. J. Alloys Compd. 2011, 509 (39), 9472–9478.
- (42) Vikhor, L. N.; Anatychuk, L. I. Theoretical Evaluation of Maximum Temperature Difference in Segmented Thermoelectric Coolers. *Appl. Therm. Eng.* **2006**, *26* (14–15), 1692–1696.
- (43) Zhang, Q.; Liao, J.; Tang, Y.; Gu, M.; Ming, C.; Qiu, P.; Bai, S.; Shi, X.; Uher, C.; Chen, L. Realizing a Thermoelectric Conversion Efficiency of 12% in Bismuth Telluride/Skutterudite Segmented Modules through Full-Parameter Optimization and Energy-Loss Minimized Integration. *Energy Environ. Sci.* **2017**, *10* (4), 956–963.
- (44) Cramer, C. L.; Wang, H.; Ma, K. Performance of Functionally Graded Thermoelectric Materials and Devices: A Review. *J. Electron. Mater.* **2018**, 47 (9), 5122–5132.
- (45) Snyder, G. J.; Toberer, E. S. Complex Thermoelectric Materials. *Nat. Mater.* **2008**, 7 (2), 105–114.
- (46) Sallehin, N. Z. I. M.; Yatim, N. M.; Suhaimi, S. A Review on Fabrication Methods for Segmented Thermoelectric Structure. *AIP Conf. Proc.* **2017**, 030003, 030003.
- (47) Seifert, W.; Ueltzen, M.; Müller, E. One-Dimensional Modelling of Thermoelectric Cooling. *Phys. Status Solidi Appl. Res.* **2002**, *194* (1), 277–290.
- (48) Thiébaut, E.; Goupil, C.; Pesty, F.; D'Angelo, Y.; Guegan, G.; Lecoeur, P. Maximization of the Thermoelectric Cooling of a Graded Peltier Device by Analytical Heat-Equation Resolution. *Phys. Rev. Appl.* **2017**, *8* (6), 064003.
- (49) Dixon, D. A.; Calabrese, J. C.; Miller, J. S. Crystal and Molecular Structure of the 2:1 Charge-Transfer Salt of Decamethylferrocene and Perfluoro-7,7,8,8-Tetracyano-p-Quinodimethane: [[Fe-(C5Me5)2]+. Cntdot.]2[TCNQF4]2-. The Electronic Structure of [TCNQF4]n (n = 0, 1-, 2-). *J. Phys. Chem.* 1989, 93 (6), 2284–2291.
- (50) Chabinyc, M. L.; Toney, M. F.; Kline, R. J.; McCulloch, I.; Heeney, M. X-Ray Scattering Study of Thin Films of Poly(2,5-Bis(3-Alkylthiophen-2-Yl)Thieno[3,2-b]Thiophene). *J. Am. Chem. Soc.* **2007**, 129 (11), 3226–3237.
- (51) DeLongchamp, D. M.; Kline, R. J.; Jung, Y.; Germack, D. S.; Lin, E. K.; Moad, A. J.; Richter, L. J.; Toney, M. F.; Heeney, M.; McCulloch, I. Controlling the Orientation of Terraced Nanoscale "Ribbons" of a Poly(Thiophene) Semiconductor. *ACS Nano* **2009**, 3 (4), 780–787.
- (52) Mcculloch, I.; Heeney, M.; Chabinyc, M. L.; Delongchamp, D.; Kline, R. J.; Cölle, M.; Duffy, W.; Fischer, D.; Gundlach, D.; Hamadani, B.; Hamilton, R.; Richter, L.; Salleo, A.; Shkunov, M.; Sparrowe, D.; Tierney, S.; Zhang, W. Semiconducting Thienothiophene Copolymers: Design, Synthesis, Morphology, and Performance in Thin-Film Organic Transistors. *Adv. Mater.* **2009**, *21* (10–11), 1091–1109.

- (53) Scholes, D. T.; Yee, P. Y.; Lindemuth, J. R.; Kang, H.; Onorato, J.; Ghosh, R.; Luscombe, C. K.; Spano, F. C.; Tolbert, S. H.; Schwartz, B. J. The Effects of Crystallinity on Charge Transport and the Structure of Sequentially Processed F 4 TCNQ-Doped Conjugated Polymer Films. *Adv. Funct. Mater.* **2017**, *27* (44), 1702654.
- (54) Kiefer, D.; Kroon, R.; Hofmann, A. I.; Sun, H.; Liu, X.; Giovannitti, A.; Stegerer, D.; Cano, A.; Hynynen, J.; Yu, L.; Zhang, Y.; Nai, D.; Harrelson, T. F.; Sommer, M.; Moulé, A. J.; Kemerink, M.; Marder, S. R.; McCulloch, I.; Fahlman, M.; Fabiano, S.; Müller, C. Double Doping of Conjugated Polymers with Monomer Molecular Dopants. *Nat. Mater.* **2019**, *18* (2), 149–155.
- (55) Liu, W.; Müller, L.; Ma, S.; Barlow, S.; Marder, S. R.; Kowalsky, W.; Köhn, A.; Lovrincic, R. Origin of the π-π Spacing Change upon Doping of Semiconducting Polymers. *J. Phys. Chem. C* **2018**, *122* (49), 27983–27990.
- (56) Tietze, M. L.; Benduhn, J.; Pahner, P.; Nell, B.; Schwarze, M.; Kleemann, H.; Krammer, M.; Zojer, K.; Vandewal, K.; Leo, K. Elementary Steps in Electrical Doping of Organic Semiconductors. *Nat. Commun.* **2018**, *9* (1), 1182.
- (57) Francis, C.; Fazzi, D.; Grimm, S. B.; Paulus, F.; Beck, S.; Hillebrandt, S.; Pucci, A.; Zaumseil, J. Raman Spectroscopy and Microscopy of Electrochemically and Chemically Doped High-Mobility Semiconducting Polymers. *J. Mater. Chem. C* **2017**, *S* (25), 6176–6184.
- (58) Fujimoto, R.; Yamashita, Y.; Kumagai, S.; Tsurumi, J.; Hinderhofer, A.; Broch, K.; Schreiber, F.; Watanabe, S.; Takeya, J. Molecular Doping in Organic Semiconductors: Fully Solution-Processed, Vacuum-Free Doping with Metal-Organic Complexes in an Orthogonal Solvent. *J. Mater. Chem. C* **2017**, *5* (46), 12023–12030
- (59) Paternò, G. M.; Robbiano, V.; Fraser, K. J.; Frost, C.; Garciá Sakai, V.; Cacialli, F. Neutron Radiation Tolerance of Two Benchmark Thiophene-Based Conjugated Polymers: The Importance of Crystallinity for Organic Avionics. Sci. Rep. 2017, 7 (1), 1–10.
- (60) Jiang, Z.; Li, X.; Strzalka, J.; Sprung, M.; Sun, T.; Sandy, A. R.; Narayanan, S.; Lee, D. R.; Wang, J. The Dedicated High-Resolution Grazing-Incidence X-Ray Scattering Beamline 8-ID-E at the Advanced Photon Source. *J. Synchrotron Radiat.* **2012**, *19* (4), 627–636.
- (61) Jiang, Z. GIXSGUI: A MATLAB Toolbox for Grazing-Incidence X-Ray Scattering Data Visualization and Reduction, and Indexing of Buried Three-Dimensional Periodic Nanostructured Films. J. Appl. Crystallogr. 2015, 48, 917–926.
- (62) Beretta, D.; Bruno, P.; Lanzani, G.; Caironi, M. Reliable Measurement of the Seebeck Coefficient of Organic and Inorganic Materials between 260 and 460 K. Rev. Sci. Instrum. 2015, 86 (7), 075104
- (63) Abadlia, L.; Gasser, F.; Khalouk, K.; Mayoufi, M.; Gasser, J. G. New Experimental Methodology, Setup and LabView Program for Accurate Absolute Thermoelectric Power and Electrical Resistivity Measurements between 25 and 1600 K: Application to Pure Copper, Platinum, Tungsten, and Nickel at Very High Temperatures. *Rev. Sci. Instrum.* 2014, 85 (9), 095121.
- (64) Schmidt, V.; Mensch, P. F. J.; Karg, S. F.; Gotsmann, B.; Das Kanungo, P.; Schmid, H.; Riel, H. Using the Seebeck Coefficient to Determine Charge Carrier Concentration, Mobility, and Relaxation Time in InAs Nanowires. *Appl. Phys. Lett.* **2014**, *104* (1), 012113.